



Cite this: *Nanoscale Adv.*, 2021, **3**, 3770

## Nickel–cobalt oxalate as an efficient non-precious electrocatalyst for an improved alkaline oxygen evolution reaction†

Sourav Ghosh, <sup>‡\*ab</sup> Rajkumar Jana, <sup>‡c</sup> Sagar Ganguli, <sup>a</sup> Harish Reddy Inta, <sup>a</sup> Gouri Tudu, <sup>a</sup> Heramba V. S. R. M. Koppisetti, <sup>a</sup> Ayan Datta <sup>\*c</sup> and Venkataramanan Mahalingam <sup>\*a</sup>

The quest for developing next-generation non-precious electrocatalysts has risen in recent times. Herein, we have designed and developed a low cost electrocatalyst by a ligand-assisted synthetic strategy in an aqueous medium. An oxalate ligand-assisted non-oxide electrocatalyst was developed by a simple wet-chemical technique for alkaline water oxidation application. The synthetic parameters for the preparation of nickel–cobalt oxalate ( $\text{Ni}_{2.5}\text{Co}_5\text{C}_2\text{O}_4$ ) were optimized, such as the metal precursor (Ni/Co) ratio, oxalic acid amount, reaction temperature, and time. Microstructural analysis revealed a mesoporous block-like architecture for nickel–cobalt oxalate ( $\text{Ni}_{2.5}\text{Co}_5\text{C}_2\text{O}_4$ ). The required overpotential of  $\text{Ni}_{2.5}\text{Co}_5\text{C}_2\text{O}_4$  for the alkaline oxygen evolution reaction (OER) was found to be 330 mV for achieving  $10 \text{ mA cm}^{-2}$ , which is superior to that of  $\text{NiC}_2\text{O}_4$ ,  $\text{CoC}_2\text{O}_4$ ,  $\text{NiCo}_2\text{O}_4$  and the state-of-the-art  $\text{RuO}_2$ . The splendid performance of  $\text{Ni}_{2.5}\text{Co}_5\text{C}_2\text{O}_4$  was further verified by its low charge transfer resistance, impressive stability performance, and 87% faradaic efficiency in alkaline medium ( $\text{pH} = 14$ ). The improved electrochemical activity was further attributed to double layer capacitance ( $C_{dl}$ ), which indefinitely divulged the inferiority of  $\text{NiCo}_2\text{O}_4$  compared to  $\text{Ni}_{2.5}\text{Co}_5\text{C}_2\text{O}_4$  for the alkaline oxygen evolution reaction (OER). The obtained proton reaction order ( $\rho_{\text{RHE}}$ ) was about 0.80, thus indicating the proton decoupled electron transfer (PDET) mechanism for OER in alkaline medium. Post-catalytic investigation revealed the formation of a flake-like porous nanostructure, indicating distinct transformation in morphology during the alkaline OER process. Further, XPS analysis demonstrated complete oxidation of  $\text{Ni}^{2+}$  and  $\text{Co}^{2+}$  centres into  $\text{Ni}^{3+}$  and  $\text{Co}^{3+}$ , respectively under high oxidation potential, thereby indicating active site formation throughout the microstructural network. Additionally, from BET-normalised LSV investigation, the intrinsic activity of  $\text{Ni}_{2.5}\text{Co}_5\text{C}_2\text{O}_4$  was also found to be higher than that of  $\text{NiCo}_2\text{O}_4$ . Finally,  $\text{Ni}_{2.5}\text{Co}_5\text{C}_2\text{O}_4$  delivered a TOF value of around  $3.28 \times 10^{-3} \text{ s}^{-1}$ , which is 5.56 fold that of  $\text{NiCo}_2\text{O}_4$  for the alkaline OER process. This report highlights the unique benefit of  $\text{Ni}_{2.5}\text{Co}_5\text{C}_2\text{O}_4$  over  $\text{NiCo}_2\text{O}_4$  for the alkaline OER. The structure–catalytic property relationship was further elucidated using density functional theory (DFT) study. To the best of our knowledge, nickel–cobalt oxalate ( $\text{Ni}_{2.5}\text{Co}_5\text{C}_2\text{O}_4$ ) was introduced for the first time as a non-precious non-oxide electrocatalyst for alkaline OER application.

Received 13th January 2021  
Accepted 27th April 2021

DOI: 10.1039/d1na00034a  
[rsc.li/nanoscale-advances](http://rsc.li/nanoscale-advances)

## 1. Introduction

Water splitting is becoming the most promising approach for hydrogen fuel production and energy storage.<sup>1–5</sup> The

requirement of a large overpotential for four electron trajectories all through the oxygen evolution reaction (OER) restricts the application in bulk mode.<sup>6,7</sup> The ideal category of catalyst for OER is still  $\text{RuO}_2$  in alkaline and  $\text{IrO}_2$  in acidic solution.<sup>8</sup> However, the cost of scalable design and availability in nature limit the use of such precious elements in day to day industrial applications. Non-precious transition metal based electrocatalysts particularly oxide and hydroxide have attracted great interest particularly owing to their simple synthetic strategy, extraordinary OER activity, and cheap market price.<sup>9,10</sup> The improved alkaline OER performance can be attributed to the corrosion resistant physicochemical properties of the working electrode leading to substantial stability in alkaline medium.<sup>11</sup> However, non-precious non-oxide transition metal based

<sup>a</sup>Department of Chemical Sciences, Indian Institute of Science Education and Research (IISER) Kolkata, Mohanpur, West Bengal 741246, India. E-mail: mvenkataramanan@yahoo.com; sourav.g1989@gmail.com

<sup>b</sup>Technical Research Centre, S. N. Bose National Centre for Basic Sciences, Block-JD, Sector-III, Salt Lake, Kolkata-700106, India

<sup>c</sup>School of Chemical Sciences, Indian Association for the Cultivation of Science, Jadavpur, Kolkata-700032, India. E-mail: spad@iacs.res.in

† Electronic supplementary information (ESI) available. See DOI: 10.1039/d1na00034a

‡ Sourav and Rajkumar contributed equally.



electrocatalysts are prone to quick *in situ* electrochemical active surface transformation, thereby rendering rapid kinetics, a low overpotential barrier and high stability. The performance of this catalytic system originates from the presence of microstructural defects, porosity and pore architecture, conductivity and oxidation (chemical) states of active elements.<sup>12–15</sup> For example, non-oxide electrocatalysts based on cobalt (Co) are well-known for their metallic nature, which encourages their wide practical application.<sup>16–18</sup> There are quite a few literature studies on non-precious non-oxide electrocatalysts for alkaline OER application, such as  $\text{Co}_4\text{N}$ ,  $(\text{Co}_{0.7}\text{Fe}_{0.3})_2\text{B}$ ,  $(\text{Co}_x\text{Fe}_{1-x})_2\text{P}$  and  $\text{Co}_{0.85}\text{Se}/\text{Co}_9\text{Se}_8$ .<sup>19–22</sup> Thus, non-precious non-oxide electrocatalysts have attracted great attention for the alkaline OER.

A ligand assisted soft-chemical strategy has been employed for the design of electrocatalysts in recent years. Feng *et al.* demonstrated an ionic liquid assisted microwave irradiation technique for the preparation of nickel–cobalt fluoride for water electrolysis.<sup>23</sup> Next, hierarchical hydrous cobalt phosphate micro-flower was employed as an efficient electrocatalyst for the alkaline OER.<sup>24</sup> Recently, our group has discussed the superior OER electrocatalytic activity of  $\text{NiCo}_2\text{O}_x\text{S}_{4-x}$  over  $\text{NiCo}_2\text{O}_4$ .<sup>25</sup> On the other hand, transition metal based oxalate is renowned as a carbon sink, suggesting it as a more sustainable way to design energy storage materials. Numerous bio- and artificial-synthesis routes have already been reported for the synthesis of oxalate anion ( $\text{C}_2\text{O}_4^{2-}$ ) from  $\text{CO}_2$ .<sup>26</sup> Therefore, utilization of oxalate-based materials is an impactful way from the clean and green synthesis viewpoint. To our knowledge, there are only few reports on oxalate based materials for OER applications. For instance, cobalt oxalate has shown promising activity as an electrocatalyst for alkaline OER applications.<sup>27,28</sup> Liu *et al.* reported the most convenient and widely used solvothermal synthetic procedure for the preparation of  $\text{CoC}_2\text{O}_4\text{-2H}_2\text{O}$  with a tuneable rod and 3-D polyhedron like morphology. Post-catalytic transformation into  $\text{CoOOH}$  species resulted in active sites for the alkaline OER with 436 and 492 mV overpotential (for 10 mA  $\text{cm}_{\text{geo}}^{-2}$ ) for the micro-rod and 3-D polyhedron respectively.<sup>29</sup> However, the high overpotential and sluggish kinetics of the catalyst are identified as major limitations for practical implementation in large scale production. To date, no such reports were found for nickel–cobalt oxalate, which might be an excellent electrocatalyst for alkaline water oxidation. In addition, fabrication of non-precious non-oxide transition metal based electrocatalysts that meet the requirement of 10 mA  $\text{cm}_{\text{geo}}^{-2}$  current density, thereby reaching a benchmark of 12% solar-to-hydrogen efficiency, is a challenging task.

Herein, we have demonstrated an oxalic acid assisted non-precious non-oxide transition metal (nickel and cobalt) based electrocatalyst for the alkaline OER. Nickel–cobalt oxalate was primarily synthesized by a wet chemical technique, followed by annealing to form nickel–cobalt oxide. The preparation technique was optimised in terms of Ni/Co ratio, oxalic acid amount, temperature and processing time. The overpotential requirement for the block-like  $\text{Ni}_{2.5}\text{Co}_5\text{C}_2\text{O}_4$  was found to be 330 mV for reaching the benchmark of 10 mA  $\text{cm}_{\text{geo}}^{-2}$ . The improved performance of the catalyst was further verified by low charge transfer resistance, long term stability and 87% faradic

efficiency. Interestingly, the control studies and the change in double layer capacitance ( $C_{\text{dl}}$ ) because of electrochemical preconditions clearly suggest that the alkaline OER catalytic performance of  $\text{Ni}_{2.5}\text{Co}_5\text{C}_2\text{O}_4$  is superior to that of its high temperature oxide counterpart *i.e.*  $\text{NiCo}_2\text{O}_4$ . The structure–catalytic property relationship was further elucidated by density functional theory (DFT) study which was performed to get insight into the improved electrochemical performance of  $\text{Ni}_{2.5}\text{Co}_5\text{C}_2\text{O}_4$  compared to the  $\text{CoC}_2\text{O}_4$ ,  $\text{NiC}_2\text{O}_4$  and  $\text{NiCo}_2\text{O}_4$ , and atomic interpretation was also proposed from computed results. In addition, electrocatalytic measurements in electrolyte solutions with different pH values were performed to understand the mechanistic details of  $\text{Ni}_{2.5}\text{Co}_5\text{C}_2\text{O}_4$  for the alkaline OER. This investigation exclusively unlocks a strategy to fabricate oxalate ligand assisted non-precious nickel–cobalt based bimetallic electrocatalysts for water oxidation application in alkaline medium.

## 2. Results and discussion

### 2.1 Structural characterization

The synthesis of nickel oxalate ( $\text{NiC}_2\text{O}_4$ ), cobalt oxalate ( $\text{CoC}_2\text{O}_4$ ) and nickel–cobalt oxalate ( $\text{Ni}_{2.5}\text{Co}_5\text{C}_2\text{O}_4$ ) samples was performed by a one-pot method using metal nitrate salts and oxalic acid in aqueous media. For comparative study, nickel cobalt oxide ( $\text{NiCo}_2\text{O}_4$ ) was prepared by calcination of nickel–cobalt oxalate ( $\text{Ni}_{2.5}\text{Co}_5\text{C}_2\text{O}_4$ ) at 350 °C for 2 h (see the details in the Experimental and Characterization section, ESI, Table S1†). The elemental phase was examined by the X-ray diffraction (XRD) method. As shown in Fig. 1a, the peak position resembles with the appearance of cobalt oxalate hydrate ( $\text{CoC}_2\text{O}_4\text{-2H}_2\text{O}$ ; ICDD no. #25-0250) and nickel oxalate hydrate ( $\text{NiC}_2\text{O}_4\text{-2H}_2\text{O}$ ; ICDD no. #01-0299). The XRD pattern of  $\text{Ni}_{2.5}\text{Co}_5\text{C}_2\text{O}_4$  is quite identical to that of phase-pure cobalt oxalate hydrate, thereby indicating the existence of substituted nickel at some portion of cobalt sites throughout the mixed-metal oxalate crystal framework.<sup>30</sup> Furthermore, the XRD pattern of a physical mixture comprising  $\text{CoC}_2\text{O}_4$  and  $\text{NiC}_2\text{O}_4$  was examined, revealing doublet peaks at 35.1° and 35.59° that can be labelled as  $\text{CoC}_2\text{O}_4$  and  $\text{NiC}_2\text{O}_4$  respectively. However,  $\text{Ni}_{2.5}\text{Co}_5\text{C}_2\text{O}_4$  shows a single broad peak around 34.9°, manifesting the (022) plane of  $\text{CoC}_2\text{O}_4$ . The resemblance of XRD patterns between  $\text{Ni}_{2.5}\text{Co}_5\text{C}_2\text{O}_4$  and  $\text{CoC}_2\text{O}_4$  further supports the existence of substituted nickel at some portion of cobalt sites throughout the mixed-metal oxalate crystal framework. In addition, the (022) peak of  $\text{Ni}_{2.5}\text{Co}_5\text{C}_2\text{O}_4$  shifts to a lower 2θ value w.r.t  $\text{CoC}_2\text{O}_4$ , revealing [022] oriented unit cell expansion due to the presence of the nickel component within the composite network (see Fig. S1, ESI†).<sup>31</sup>

Thermal stability of the as-prepared sample was corroborated by DTA-TG analysis. Fig. 1b shows an endothermic peak around 205 °C, indicating the removal of lattice water, resulting in 19% weight loss. The exothermic peak around 294 °C represents the decomposition of oxalate ligand with a 57% weight loss compared to the as-prepared mixed oxalate sample.<sup>32</sup> No further weight loss is observed in the 300 to 600 °C temperature range. Thus, for the preparation of the  $\text{NiCo}_2\text{O}_4$



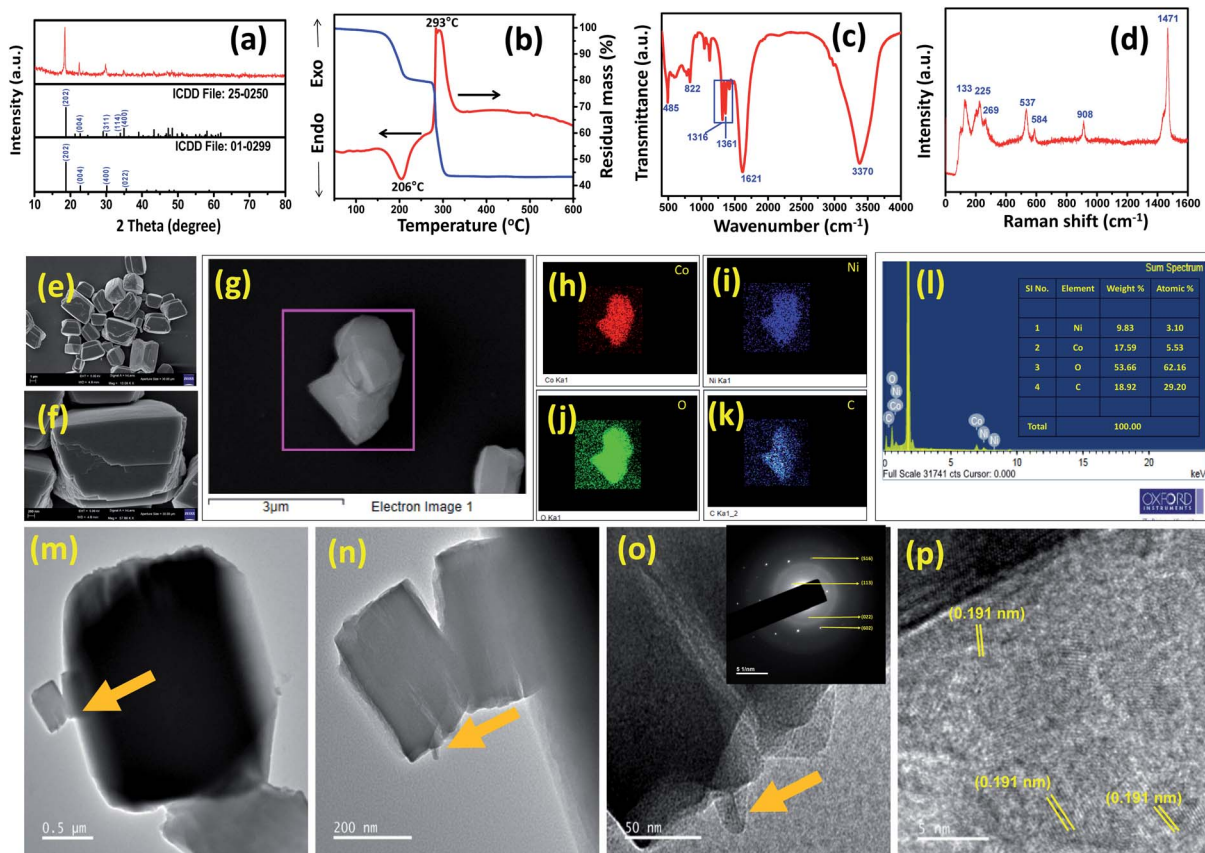


Fig. 1 (a) PXRD with the standard patterns of  $\text{NiC}_2\text{O}_4\text{-}2\text{H}_2\text{O}$  (ICDD no. 01-0299) and  $\text{CoC}_2\text{O}_4\text{-}2\text{H}_2\text{O}$  (ICDD no. 25-0250), (b) DTA-TG, (c) FTIR and (d) Raman pattern of the as-prepared nickel–cobalt oxalate ( $\text{Ni}_{2.5}\text{Co}_5\text{C}_2\text{O}_4$ ) sample. Morphological study including (e and f) FESEM images, (g–k) elemental mapping, (l) EDS study, (m–o) TEM images (the inset showing SAED) and (p) HRTEM image of the as-prepared nickel–cobalt oxalate ( $\text{Ni}_{2.5}\text{Co}_5\text{C}_2\text{O}_4$ ) sample.

sample, the as-prepared  $\text{Ni}_{2.5}\text{Co}_5\text{C}_2\text{O}_4$  was calcined at  $350\text{ }^\circ\text{C}$ . Fourier-transform infrared (FTIR) spectroscopy study was carried out for further structural characterization of the sample (Fig. 1c). The FTIR peak positioned around  $485\text{ cm}^{-1}$  is assigned to metal–oxygen vibration mode. The C–O vibration mode is obtained around  $1316$  (symmetric) and  $1361\text{ cm}^{-1}$  (asymmetric) along with a strong vibrational band at  $1621\text{ cm}^{-1}$ , which is a signature characteristic peak for carbonyl stretching vibrational mode, confirming the presence of the oxalate moiety in the as-prepared sample.<sup>29</sup> The broad vibrational band around  $3370\text{ cm}^{-1}$  is attributed to water molecules, while  $822\text{ cm}^{-1}$  is to asymmetric O–C–O vibrational mode. Raman measurements were also performed to obtain more structural information (Fig. 1d). The intense peak around  $912\text{ cm}^{-1}$  is attributed to C–C stretching mode, which is IR-silent. The presence of C–C–O bending mode is concluded from the observed  $532\text{ cm}^{-1}$  peak. In addition, appearance of peaks around  $225$  and  $266\text{ cm}^{-1}$  is ascribed to M–O stretching and O–M–O ring-bending modes respectively, where M stands for the metal centre (cobalt and nickel).<sup>16,33</sup> The XPS technique was employed for the analysis of chemical state and probable elemental composition of the as-prepared sample (see Fig. S2, ESI†). The C 1s spectrum exhibits peaks around  $286.48$ ,  $287.69$  and  $290.3\text{ eV}$  particularly

for C–O, C=O and C–F respectively (see Fig. S2a, ESI†). The appearance of  $290.3\text{ eV}$  binding energy could originate from Nafion residue which is used as a binder.<sup>34,35</sup> As shown in Fig. S2b (ESI†), peaks at  $782.93$  and  $798.87\text{ eV}$  can be designated as Co  $2p_{3/2}$  and Co  $2p_{1/2}$ , respectively with a clear separation of  $15.94\text{ eV}$ , confirming the presence of  $\text{Co}^{2+}$ .<sup>36</sup> The satellite signals around  $786.79$  and  $803.86\text{ eV}$  further support the same (see Fig. S2b, ESI†). The presence of  $\text{Ni}^{2+}$  can be suspected from the binding energy peaks around  $857.71$  and  $875.35\text{ eV}$  assigned to Ni  $2p_{3/2}$  and Ni  $2p_{1/2}$  respectively, along with satellite peaks at  $862.61$  and  $881.14\text{ eV}$  (see Fig. S2c, ESI†).<sup>37</sup> The narrow scan of the O 1s peak is deconvoluted into two peaks at  $533.62$  and  $534.65\text{ eV}$  representing C–O and lattice water molecules, respectively (see Fig. S2d, ESI†).<sup>38</sup> Inductively coupled plasma-atomic emission spectroscopy (ICP-AES) was also employed to get quantitative information regarding the elemental composition of  $\text{Ni}_{2.5}\text{Co}_5\text{C}_2\text{O}_4$ . The Ni/Co ratio is found to be  $1:2.018$  (see Table S2, ESI†).

## 2.2 Morphological characterization

Microstructural analysis was performed by FESEM and TEM investigation. The displayed FESEM image presents block shaped nanostructures of  $\text{Ni}_{2.5}\text{Co}_5\text{C}_2\text{O}_4$  (Fig. 1e and f). Close



inspection reveals a smooth surface along with a clear boundary, thereby indicating sturdy close-packed interaction among the crystallites. Elemental distribution was further determined by energy-dispersive X-ray spectroscopy (EDS) and mapping investigation (Fig. 1g–l). It shows uniform spreading of Ni and Co throughout the framework with a Ni/Co ratio of about 1 : 2. TEM study also shows a block-like morphology, which is formed from self-assembly of porous sheet-like nanostructures (Fig. 1m–o). The selected area electron diffraction (SAED) image indeed shows crystalline features of the sample which is further confirmed by 0.191 nm interplanar distance, indicating the (602) plane from HRTEM analysis (Fig. 1o and p). To study the morphological evolution, time dependent synthesis was carried out at different time intervals from 15 min to 60 min (see Fig. S3, ESI†). However, no specific change in morphology was observed from 15 min to 2 h. As a control experiment, phase pure  $\text{CoC}_2\text{O}_4$ ,  $\text{NiC}_2\text{O}_4$  and  $\text{NiCo}_2\text{O}_4$  samples were prepared and subjected to microstructural analysis. Fig. S4a–c (ESI†) shows the nano-rod like architecture of  $\text{CoC}_2\text{O}_4$  with a smooth surface. The TEM image presents a controllable 1-D microstructure with 150–250 nm diameter (see Fig. S5a–c, ESI†). The HRTEM image indicates 0.296 nm lattice fringes for the (400) plane (see Fig. S3d, ESI†).  $\text{NiC}_2\text{O}_4$  reveals an irregular sheet-like architecture with a packed-surface, thus further indicating that nano-block units self-assembled to grow such an architecture (see Fig. S6a–c, ESI†). TEM investigation demonstrates the formation of sheet-like nanostructures with 0.390 nm interplanar spacing of the (004) plane (see Fig. S7a–d, ESI†). For comparison,  $\text{NiCo}_2\text{O}_4$  was synthesized by high-temperature thermal treatment of the as-prepared  $\text{Ni}_{2.5}\text{Co}_5\text{C}_2\text{O}_4$ . The XRD pattern confirms the formation of phase pure  $\text{NiCo}_2\text{O}_4$  and absence of any impurity phase such as  $\text{NiO}$  and  $\text{Co}_3\text{O}_4$  (see Fig. S8a, ESI†). FESEM study reveals a block-like nano-porous network, thus indicating the formation of porosity due to thermal decomposition of oxalate during the high temperature treatment (see Fig. S8b and c, ESI†). EDS and elemental mapping indicate the distribution of Ni and Co throughout the framework with a Ni/Co ratio of about 1 : 2, which is further supported by ICP-AES analysis (see Fig. S8d–j, Table S3, ESI†). The TEM image indicates a micro-sheet like framework with 0.234 and 0.245 nm lattice fringes for (222) and (311) planes respectively (see Fig. S9a–d, ESI†). Close inspection shows that small nanoparticles assembled together to form a micro-sheet like architecture, leading to uniform distribution of interparticle porosity.

### 2.3 Electrochemical study

To investigate the electrochemical activity, working electrodes were prepared with different loading amounts of  $\text{Ni}_{2.5}\text{Co}_5\text{C}_2\text{O}_4$  by the drop-casting technique. As shown in Fig. 2a, the best performance is obtained for 4 mg  $\text{cm}^{-2}$  catalyst loading using carbon paper as the substrate. For the benchmark value of 10 mA  $\text{cm}^{-2}$ ,  $\text{Ni}_{2.5}\text{Co}_5\text{C}_2\text{O}_4$  consumes 330 mV overpotential for 4 mg  $\text{cm}^{-2}$  catalyst loading (see Table S4, ESI†).<sup>39</sup> However, the catalytic activity of the carbon paper supported electrocatalyst was also compared to that obtained with glassy carbon as the

substrate. As displayed in Fig. S10,† the glassy carbon drop-cast electrocatalyst showed lower mass activity at 1.7 V vs. RHE, showing the contribution from the porous network of carbon paper that could lead to better electrolyte diffusion for improved electrocatalytic performance of the  $\text{Ni}_{2.5}\text{Co}_5\text{C}_2\text{O}_4$  sample. However, a comparative study was also carried out with this optimized loading of 4 mg  $\text{cm}^{-2}$  for carbon paper supported reference samples such as  $\text{CoC}_2\text{O}_4$ ,  $\text{NiC}_2\text{O}_4$  and standard  $\text{RuO}_2$ . To investigate the electrochemical features, the CV technique was used with correction for uncompensated solution resistance ( $R_u$ ) for all the electrocatalysts (Fig. S11†). The overpotential to reach the benchmark of 10 mA  $\text{cm}^{-2}$  is 370, 540 and 350 mV for  $\text{CoC}_2\text{O}_4$ ,  $\text{NiC}_2\text{O}_4$  and standard  $\text{RuO}_2$ , respectively (Fig. 2b). Again, the OER activity of  $\text{Ni}_{2.5}\text{Co}_5\text{C}_2\text{O}_4$  is superior compared to that of  $\text{NiCo}_2\text{O}_4$ , which requires 410 mV overpotential for reaching 10 mA  $\text{cm}^{-2}$ . The Tafel plot was recorded to study the OER kinetics of electrocatalysts. Fig. 2c shows a lower value of the Tafel slope for  $\text{Ni}_{2.5}\text{Co}_5\text{C}_2\text{O}_4$  (81 mV  $\text{dec}^{-1}$ ) compared to control samples, such as  $\text{CoC}_2\text{O}_4$  (90 mV  $\text{dec}^{-1}$ ),  $\text{NiC}_2\text{O}_4$  (229 mV  $\text{dec}^{-1}$ ) and  $\text{NiCo}_2\text{O}_4$  (121 mV  $\text{dec}^{-1}$ ), suggesting the relatively rapid kinetics for  $\text{Ni}_{2.5}\text{Co}_5\text{C}_2\text{O}_4$  compared to others.<sup>35</sup> However, the state-of-the-art  $\text{RuO}_2$  electrocatalyst exhibited 79 mV  $\text{dec}^{-1}$  Tafel slope, which is the best among all the samples (see Table S5, ESI†). Composition optimization was performed with the variation of Ni/Co amount, and the best activity was observed for a Ni/Co ratio of about 2.5/5, which is indexed as  $\text{Ni}_{2.5}\text{Co}_5\text{C}_2\text{O}_4$  (see Fig. 2d, S12a and Table S6, ESI†). Thereafter, the process parameter for the synthesis of the  $\text{Ni}_{2.5}\text{Co}_5\text{C}_2\text{O}_4$  catalyst was further optimized, such as the amount of oxalic acid, reaction temperature and time. The best performance was obtained with 12 mmol oxalic acid, 80 °C reaction temperature and 2 hours reaction time (see Fig. S12b–d and Tables S7–S9, ESI†). In addition, the OER mechanism for  $\text{Ni}_{2.5}\text{Co}_5\text{C}_2\text{O}_4$  was investigated with the variation of pH of electrolytes (12, 12.5, 13, 13.5 and 14) under alkaline conditions (Fig. 2e). Proton reaction order is considered as the most convenient parameter to study the mechanistic pathway and estimated from the following equation:

$$\rho_{\text{RHE}} = \left( \frac{\partial \log(j)}{\partial \text{pH}} \right)_E = - \left( \frac{\partial E}{\partial \text{pH}} \right)_j \Big/ \left( \frac{\partial E}{\partial \log(j)} \right)_{\text{pH}}$$

where  $\rho_{\text{RHE}}$  refers to the proton reaction order on the RHE scale.<sup>40</sup> The result suggests that the proton reaction order ( $\rho_{\text{RHE}}$ ) for the  $\text{Ni}_{2.5}\text{Co}_5\text{C}_2\text{O}_4$  is 0.80, thus proposing proton decoupled electron transfer (PDET) trajectory for the alkaline OER process (Fig. 2f). The deprotonation pathway is presumed to proceed as follows:  $\text{OOH}_{(\text{ads})} + \text{OH}^- \rightarrow \text{OO}_{(\text{ads})} + \text{H}^+ + \text{e}^-$  and the decoupling assisted deprotonation mechanism is most consistent with it.<sup>41</sup>

Fig. S13† presents the magnified CV data for both  $\text{Ni}_{2.5}\text{Co}_5\text{C}_2\text{O}_4$  and  $\text{NiCo}_2\text{O}_4$  samples. From the as-displayed oxidation and reduction peaks, higher current density and peak area are noted for the  $\text{Ni}_{2.5}\text{Co}_5\text{C}_2\text{O}_4$  compared to  $\text{NiCo}_2\text{O}_4$ . This also indicates that improved geometric OER performance may be attributed to the presence of more number of accessible active sites in the alkaline medium for the  $\text{Ni}_{2.5}\text{Co}_5\text{C}_2\text{O}_4$  sample.<sup>42</sup> Further, the requirement of 10 mA  $\text{cm}^{-2}$  was achieved at 1.56 V

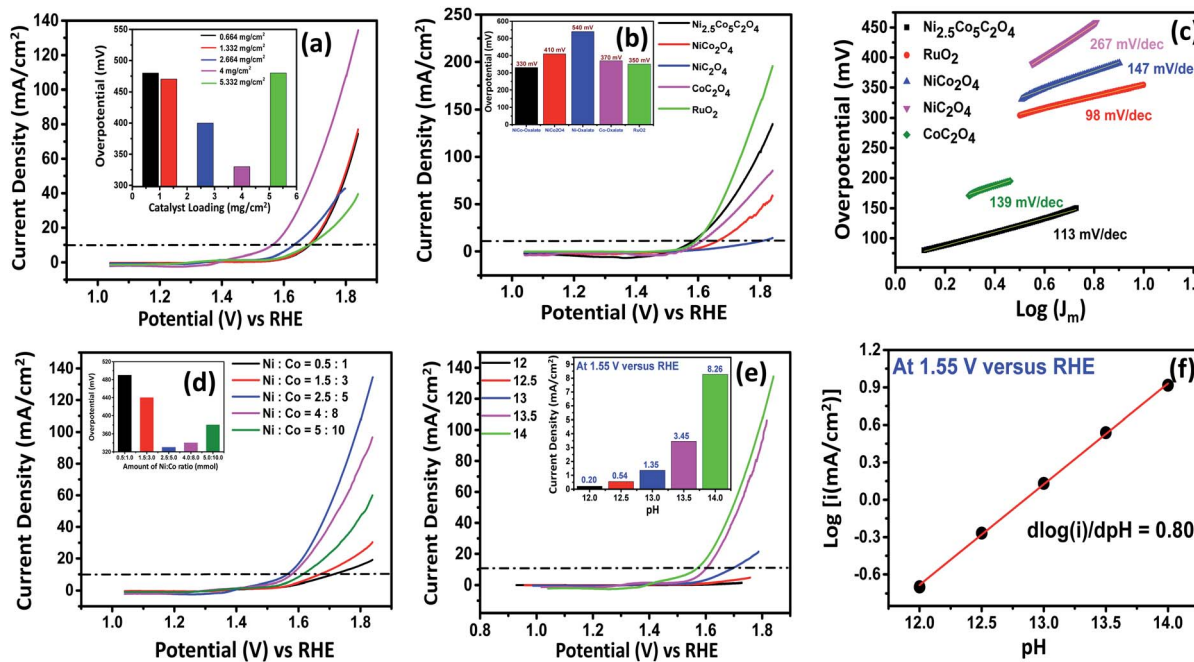


Fig. 2 (a)  $iR$ -corrected LSV scan for different loading amounts for  $\text{Ni}_{2.5}\text{Co}_5\text{C}_2\text{O}_4$ , (b)  $iR$ -corrected LSV scan for different electrocatalysts [the inset showing the overpotential value to reach the benchmark of  $10 \text{ mA cm}^{-2}_{\text{geo}}$ ], (c) Tafel slope analysis of different electrocatalysts, (d)  $iR$ -corrected LSV scan for different Ni/Co ratios, (e) LSV scan and (f) linear fit of  $\text{Ni}_{2.5}\text{Co}_5\text{C}_2\text{O}_4$  with the variation of pH.

vs. RHE for  $\text{Ni}_{2.5}\text{Co}_5\text{C}_2\text{O}_4$ , whereas  $\text{NiCo}_2\text{O}_4$  delivered  $1.64 \text{ V}$  vs. RHE for the same. It unequivocally implies the higher geometrical OER activity of  $\text{Ni}_{2.5}\text{Co}_5\text{C}_2\text{O}_4$  than  $\text{NiCo}_2\text{O}_4$ . To gather further support, double layer capacitance ( $C_{\text{dl}}$ ) was calculated that was indefinitely assumed as a non-destructive parameter for the electrochemical active surface area (ECSA) calculations.<sup>43</sup> The  $C_{\text{dl}}$  value for  $\text{Ni}_{2.5}\text{Co}_5\text{C}_2\text{O}_4$  is calculated to be  $1.31 \text{ mF cm}^{-2}$ , whereas  $\text{NiCo}_2\text{O}_4$  shows  $2.84 \text{ mF cm}^{-2}$  just before precondition (Fig. 3a and d). However, the  $C_{\text{dl}}$  value is significantly increased up to  $10.61 \text{ mF cm}^{-2}$  after electrochemical precondition for  $\text{Ni}_{2.5}\text{Co}_5\text{C}_2\text{O}_4$ , while the corresponding value for  $\text{NiCo}_2\text{O}_4$  remains nearly the same at  $2.93 \text{ mF cm}^{-2}$  (Fig. 3b and e). Thus development of a higher number of

accessible active sites is observed during electrochemical precondition for  $\text{Ni}_{2.5}\text{Co}_5\text{C}_2\text{O}_4$  compared to the  $\text{NiCo}_2\text{O}_4$  sample (Fig. 3c and f).<sup>44</sup> This also suggests more ECSA and thus more surface coverage ( $\theta$ ) that provides a higher value of current ( $j$ ) according to the following expression:

$$j = [\text{OH}^-] \times \theta \times e^{-\frac{\Delta G}{RT}}$$

where the current ( $j$ ) value is directly proportional to surface coverage ( $\theta$ ) involving  $^{*}\text{OOH}$  or  $^{*}\text{OH}$  sites,  $[\text{OH}^-]$  concentration and exponential factor which actually depends on the adsorbed surface of intermediate species for the alkaline OER.<sup>40</sup> The change in  $C_{\text{dl}}$  is also estimated for  $\text{CoC}_2\text{O}_4$  and  $\text{NiC}_2\text{O}_4$  samples that further supports the better electrochemical performance of  $\text{CoC}_2\text{O}_4$  compared to  $\text{NiC}_2\text{O}_4$  for the alkaline OER (see Fig. S14 and S15, ESI†).

To further study the electrochemical properties, electrochemical impedance spectroscopy (EIS) was employed to evaluate the charge transfer resistance ( $R_{\text{ct}}$ ) and transport kinetics. As expected,  $\text{Ni}_{2.5}\text{Co}_5\text{C}_2\text{O}_4$  delivers a lower  $R_{\text{ct}}$  value of about  $6.34 \text{ ohm}$  in comparison with  $\text{NiCo}_2\text{O}_4$  ( $26.14 \text{ ohm}$ ), thereby indicating the occurrence of rapid charge transport phenomena for  $\text{Ni}_{2.5}\text{Co}_5\text{C}_2\text{O}_4$  (Fig. 4a).<sup>45</sup> Likewise,  $\text{NiC}_2\text{O}_4$  shows a higher  $R_{\text{ct}}$  value than  $\text{CoC}_2\text{O}_4$ , justifying the higher conducting behaviour of  $\text{CoC}_2\text{O}_4$  in alkaline medium (see Fig. S16, ESI†). To study the intrinsic activity of the drop-cast catalyst, BET normalized electrochemical performance was already reported as the most convenient analytical technique by Shao-Horn and co-workers.<sup>46</sup> As shown in Fig. 4b, the nitrogen adsorption–desorption isotherm displays a type-IV isotherm and H-3 hysteresis, reflecting a mesoporous network and slit-like pore geometry

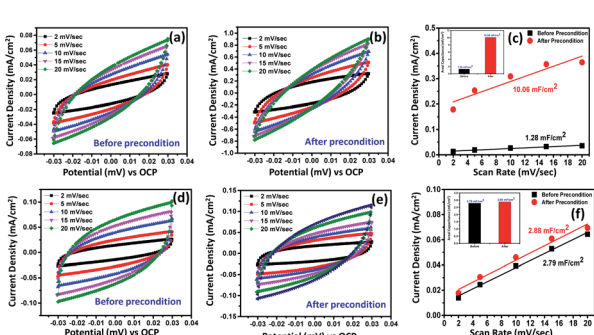


Fig. 3 CV curves recorded at different scan rates to estimate the double layer capacitance ( $C_{\text{dl}}$ ) for (a and b)  $\text{Ni}_{2.5}\text{Co}_5\text{C}_2\text{O}_4$  and (d and e)  $\text{NiCo}_2\text{O}_4$ . Linear fit for the estimation of double layer capacitance ( $C_{\text{dl}}$ ) from the DLC current vs. scan rate plot for (c)  $\text{Ni}_{2.5}\text{Co}_5\text{C}_2\text{O}_4$  and (f)  $\text{NiCo}_2\text{O}_4$ .



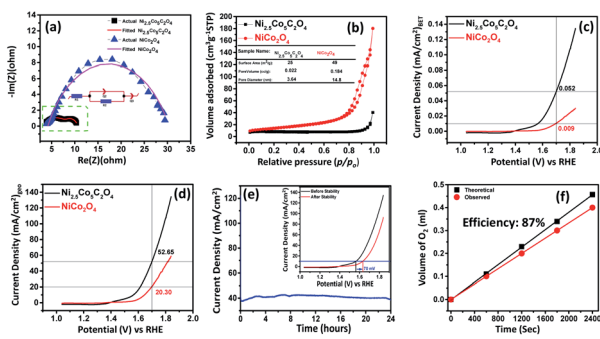


Fig. 4 (a) Nyquist plots of different electrocatalysts, (b) N<sub>2</sub> adsorption-desorption isotherm of Ni<sub>2.5</sub>Co<sub>5</sub>C<sub>2</sub>O<sub>4</sub> and NiCo<sub>2</sub>O<sub>4</sub> samples, catalytic performance in terms of (c) BET surface area normalised LSV plot and (d) geometrical area normalised LSV plot for Ni<sub>2.5</sub>Co<sub>5</sub>C<sub>2</sub>O<sub>4</sub> and NiCo<sub>2</sub>O<sub>4</sub> samples, (e) stability study of the best catalyst Ni<sub>2.5</sub>Co<sub>5</sub>C<sub>2</sub>O<sub>4</sub> [the inset showing the overpotential value to reach the benchmark of 10 mA cm<sup>-2</sup>], and (f) analysis of faradaic efficiency for the Ni<sub>2.5</sub>Co<sub>5</sub>C<sub>2</sub>O<sub>4</sub>.

respectively.<sup>47</sup> The BET surface area is found to be 25 and 49 m<sup>2</sup> g<sup>-1</sup> for Ni<sub>2.5</sub>Co<sub>5</sub>C<sub>2</sub>O<sub>4</sub> and NiCo<sub>2</sub>O<sub>4</sub> respectively, which could be attributed to thermal decomposition of oxalate ligand during calcination treatment at high-temperature. Fig. 4c presents the comparative survey of intrinsic alkaline OER performance for both the samples. From the BET normalized LSV plot, Ni<sub>2.5</sub>Co<sub>5</sub>C<sub>2</sub>O<sub>4</sub> shows a current density of about 0.052 mA cm<sub>BET</sub><sup>-2</sup>, which is 5.7 fold greater than that of NiCo<sub>2</sub>O<sub>4</sub> at 1.7 V vs. RHE. In addition, the geometrical performance of Ni<sub>2.5</sub>Co<sub>5</sub>C<sub>2</sub>O<sub>4</sub> is also superior to that of NiCo<sub>2</sub>O<sub>4</sub> for the OER in alkaline medium (Fig. 4d). This result indicates the superiority of Ni<sub>2.5</sub>Co<sub>5</sub>C<sub>2</sub>O<sub>4</sub> over its widely used high temperature calcined product of NiCo<sub>2</sub>O<sub>4</sub> from both intrinsic and geometrical aspects for the OER under alkaline conditions.<sup>48</sup> To evaluate the applicability for long-term usage, the stability test of the Ni<sub>2.5</sub>Co<sub>5</sub>C<sub>2</sub>O<sub>4</sub> catalyst was performed for 24 hours by the chronoamperometry technique (Fig. 4e). Alkaline OER performance is relatively stable up to the initial 12 hours of the experiment; thereafter, the performance slightly decreased with time. After the stability test, the Ni<sub>2.5</sub>Co<sub>5</sub>C<sub>2</sub>O<sub>4</sub> sample achieves 10 mA cm<sub>geo</sub><sup>-2</sup> with around 350 mV overpotential, which is roughly 20 mV more than that of the as-prepared electrocatalyst (inset of Fig. 4e). Interestingly, the Ni/Co ratio is found to be 1 : 2.38, indicating mechanical inertness of the electrocatalyst even after the long-term 24 h stability test at pH = 14.

Finally, faradaic efficiency was studied and the obtained value for Ni<sub>2.5</sub>Co<sub>5</sub>C<sub>2</sub>O<sub>4</sub> is 87% (Fig. 4f). It indeed denotes sufficiently high activity of the electrocatalyst for alkaline water oxidation reaction. Turnover frequency (TOF) is one of the essential parameters to examine the intrinsic performance of the electrocatalyst. The TOF is expressed as follows:

$$\text{TOF} = j \frac{\text{SA}_{\text{geo}}}{4F}$$

where  $F$ ,  $n$  and  $j$  denote the Faraday constant (96 485 C mol<sup>-1</sup>), moles of the catalytically active species and geometrical area (SA<sub>geo</sub>) normalized current density (mA cm<sup>-2</sup>)<sub>geo</sub>.<sup>49</sup> The amount

of active elemental species was calculated from ICP-AES study (see Tables S2 and S3, ESI<sup>†</sup>). The TOF value is found to be  $3.28 \times 10^{-3}$  s<sup>-1</sup> for Ni<sub>2.5</sub>Co<sub>5</sub>C<sub>2</sub>O<sub>4</sub>, whereas the value for NiCo<sub>2</sub>O<sub>4</sub> is  $5.89 \times 10^{-4}$  s<sup>-1</sup> at 1.63 V vs. RHE, indicating 5.56 fold increased intrinsic superiority of Ni<sub>2.5</sub>Co<sub>5</sub>C<sub>2</sub>O<sub>4</sub> over NiCo<sub>2</sub>O<sub>4</sub>, which is also previously supported by BET normalised LSV investigation. Furthermore, the electrochemical activity of Ni<sub>2.5</sub>Co<sub>5</sub>C<sub>2</sub>O<sub>4</sub> is almost found to be comparable with that of earlier reported non-precious electrocatalysts and standard RuO<sub>2</sub> for the alkaline OER (see Table S10, ESI<sup>†</sup>).<sup>19-24,29,50-53</sup>

## 2.4 Post-catalytic analysis

To understand the post-catalytic transformation, the carbon paper supported catalyst was subjected to composition and microstructural analysis. As evident from Fig. S17 (ESI<sup>†</sup>), no characteristic XRD pattern of the post-catalytic sample is observed except the sharp conspicuous diffraction signal which is assigned to the peaks from carbon paper. However, XPS measurements clearly show the structural features and elemental composition of the post-catalytic sample (see Fig. S18, ESI<sup>†</sup>). The C 1s pattern shows the appearance of two new signals around 291.77 and 294.76 eV, indicating the existence of a K<sup>+</sup> adsorbed microstructural framework for the post-catalytic sample (see Fig. S18a, ESI<sup>†</sup>).<sup>37</sup> From the Co 2p narrow scan, the peaks around 780.25 and 796.15 eV could corroborate the existence of Co<sup>3+</sup> in the post-catalytic network (see Fig. S18b, ESI<sup>†</sup>).<sup>36</sup> Further, the presence of satellite peaks around 785.33 and 802.35 eV confirms the same.<sup>54</sup> Likewise, distinct XPS signals around 855.95 and 874.1 eV along with satellite peaks around 861.54 and 880.01 eV confirm the presence of Ni<sup>3+</sup> (see Fig. S18c, ESI<sup>†</sup>).<sup>37</sup> However, the O 1s spectrum shows peaks around 530.01, 531.08 and 534.69 eV particularly for lattice oxygen, hydroxyl groups (adsorbed) and lattice water molecules respectively (see Fig. S18d, ESI<sup>†</sup>). Thus, composition analysis clearly shows that almost all Ni<sup>2+</sup> and Co<sup>2+</sup> oxidizes into Ni<sup>3+</sup> and Co<sup>3+</sup> respectively under high oxidation potential gradient during the OER process. Furthermore, inductively coupled plasma-atomic emission spectroscopy (ICP-AES) study reveals a Ni/Co ratio of about 1 : 2.15 for the post-catalyst sample, thereby confirming the absence of any such metal ion leaching during the OER for Ni<sub>2.5</sub>Co<sub>5</sub>C<sub>2</sub>O<sub>4</sub> that further confirms the mechanical stability of the working electrode in alkaline medium. The morphology of the post-OER sample was investigated by FESEM and TEM. The FESEM image shows flake-like assembly, which confirms structural transformation from a block to flake-like nanostructure under alkaline OER conditions (see Fig. S19a-d, ESI<sup>†</sup>). In addition, TEM investigation displays microstructural aggregation throughout the mesoporous network of the post-catalytic sample with lattice fringes of 0.220 nm representing the (006) plane of CoOOH (ICDD no. 014-0673).<sup>48</sup> EDS and elemental mapping further reveal the uniform spreading of Ni, Co, C and O for the post-catalytic sample (see Fig. S19e-j, ESI<sup>†</sup>). For further validation, Raman measurements were performed to examine the *in situ* transformation of the catalyst during electrochemical precondition treatment. The Raman signals appear at 186, 470, 510 and



666 cm<sup>-1</sup> for A<sub>g</sub>, E<sub>g</sub>, F<sub>2g</sub> and A<sub>1g</sub> respectively, confirming the formation of oxyhydroxide species from nickel cobalt oxalate (see Fig. S20, ESI<sup>†</sup>).<sup>20,29</sup>

## 2.5 Computational study

To get better insight into the structure–catalytic property relationship of the designed materials, we have performed density functional theory (DFT) study based on first-principles calculations using the Vienna *Ab Initio* Simulation Package (VASP).<sup>55</sup> As revealed from PXRD analysis, the highest intensity planes namely (311) for NiCo<sub>2</sub>O<sub>4</sub> and (202) for NiC<sub>2</sub>O<sub>4</sub>, CoC<sub>2</sub>O<sub>4</sub> and Ni<sub>2.5</sub>Co<sub>5</sub>C<sub>2</sub>O<sub>4</sub> are considered to be the active planes for the electrochemical OER and all the DFT studies were performed on NiCo<sub>2</sub>O<sub>4</sub> (311), NiC<sub>2</sub>O<sub>4</sub> (202), CoC<sub>2</sub>O<sub>4</sub> (202) and Ni<sub>2.5</sub>Co<sub>5</sub>C<sub>2</sub>O<sub>4</sub> (202) surfaces. The NiCo<sub>2</sub>O<sub>4</sub> (311) surface contains surface exposed Ni<sup>2+</sup> and Co<sup>3+</sup> ions which are bi and tri-coordinated respectively while both NiC<sub>2</sub>O<sub>4</sub> (202) and CoC<sub>2</sub>O<sub>4</sub> (202) surfaces consist of tri-coordinated surface exposed Ni<sup>2+</sup> and Co<sup>2+</sup> respectively (see Fig. S21a–c, ESI<sup>†</sup>). On the contrary, the Ni<sub>2.5</sub>Co<sub>5</sub>C<sub>2</sub>O<sub>4</sub> (202) surface contains both surface exposed Ni<sup>2+</sup> and Co<sup>2+</sup> (see Fig. S21d, ESI<sup>†</sup>). However, all of the oxalates have bulk tetra and penta-coordinated Ni<sup>2+</sup> and Co<sup>2+</sup> ions (see Fig. S21, ESI<sup>†</sup>). The M–OH bond strength for the metal-based electrocatalysts is considered to be the key descriptor for OER activity.<sup>56–60</sup> The weaker the M–OH bond strength, the higher will be the activity. The more stable OH adsorption site for the NiCo<sub>2</sub>O<sub>4</sub> (311) surface is Co<sup>3+</sup> with a binding energy (B. E.) of −0.65 eV while those for NiC<sub>2</sub>O<sub>4</sub> and CoC<sub>2</sub>O<sub>4</sub> (202) surfaces are −1.15 and −0.46 eV respectively (see Fig. 5a–c, S22 and Table S11, ESI<sup>†</sup>). On the other hand, tri-coordinated surface Ni<sup>2+</sup> ion is

the most stable site for OH adsorption with a B.E. of −0.23 eV (see Fig. S23 and Table S11, ESI<sup>†</sup>). Hence, the M–OH bond strength follows the order Ni<sub>2.5</sub>Co<sub>5</sub>C<sub>2</sub>O<sub>4</sub> (202) < CoC<sub>2</sub>O<sub>4</sub> (202) < NiC<sub>2</sub>O<sub>4</sub> (311) < NiC<sub>2</sub>O<sub>4</sub> (202). In addition, Bader charge analysis<sup>61,62</sup> exhibits a charge transfer of 0.28|e| from adsorbed OH (OH<sup>\*</sup>) to the Ni<sub>2.5</sub>Co<sub>5</sub>C<sub>2</sub>O<sub>4</sub> (202) catalyst surface, indicating relatively weaker charge transfer interaction compared to CoC<sub>2</sub>O<sub>4</sub> (0.4|e|), NiC<sub>2</sub>O<sub>4</sub> (0.65|e|) and NiC<sub>2</sub>O<sub>4</sub> (0.84|e|) surfaces. The charge density difference (CDD) plot further confirms the charge transfer from OH<sup>\*</sup> to different surfaces (Fig. S24<sup>†</sup>). Therefore, with relatively weaker M–OH bonding interaction, the Ni<sub>2.5</sub>Co<sub>5</sub>C<sub>2</sub>O<sub>4</sub> (202) catalyst surface is superior to the other surfaces and consequently the order of OER activity is found to be NiC<sub>2</sub>O<sub>4</sub> (202) < NiCo<sub>2</sub>O<sub>4</sub> (311) < CoC<sub>2</sub>O<sub>4</sub> (202) < Ni<sub>2.5</sub>Co<sub>5</sub>C<sub>2</sub>O<sub>4</sub> (202), which very nicely corroborates the experimental findings (*vide infra*). The bonding interaction between adsorbed OH and interacting Ni in OH<sup>\*</sup>–Ni<sub>2.5</sub>Co<sub>5</sub>C<sub>2</sub>O<sub>4</sub> (202) can be further confirmed from the density of states (DOS) plot (asterisk indicates the contribution from O-2p) as shown in Fig. 5d. The generation of the O-2p state can be clearly visualized near −5.95 eV (as marked with a black box) in the DOS plot for OH<sup>\*</sup>–Ni<sub>2.5</sub>Co<sub>5</sub>C<sub>2</sub>O<sub>4</sub> (202) (Fig. 5e). Besides, projected density of states (PDOS) analysis further confirms the bonding interaction between O-2p<sub>z</sub> and Ni-d<sub>xy</sub> orbitals which indicates that hybridization mainly occurs between these orbitals (Fig. 5f).

From the above discussion, it can be concluded that the adsorption of OH is weaker on the Ni<sub>2.5</sub>Co<sub>5</sub>C<sub>2</sub>O<sub>4</sub> (202) catalyst surface and hence exhibiting better OER activity and this conclusion can be further justified by a d-band model which correlates the d-band centre (DBC) with the adsorption energies of the intermediates (here OH).<sup>63–65</sup> The positions of DBCs are

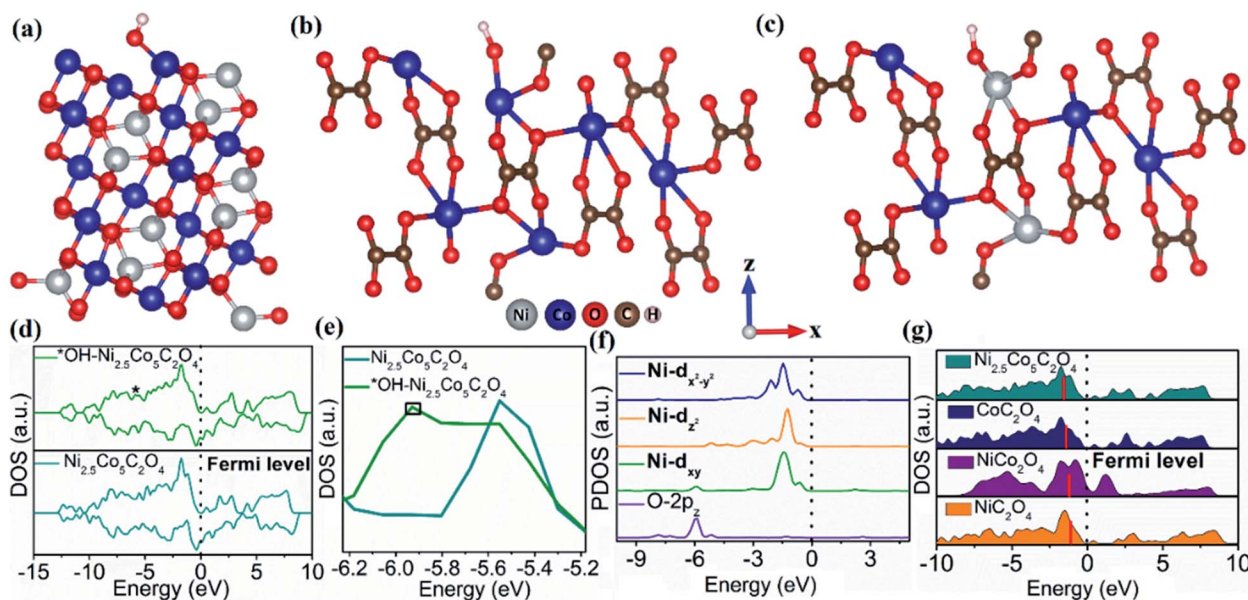


Fig. 5 Optimized structure of OH\* adsorbed (a) NiCo<sub>2</sub>O<sub>4</sub> (311), (b) CoC<sub>2</sub>O<sub>4</sub> (202), and (c) Ni<sub>2.5</sub>Co<sub>5</sub>C<sub>2</sub>O<sub>4</sub> (202) surfaces, (d) DOS plots for Ni<sub>2.5</sub>Co<sub>5</sub>C<sub>2</sub>O<sub>4</sub> (202) and OH<sup>\*</sup>–Ni<sub>2.5</sub>Co<sub>5</sub>C<sub>2</sub>O<sub>4</sub> (202) surfaces (asterisk indicates the contribution from O-2p), (e) magnified DOS (the O-2p state is situated at around −5.95 eV as marked by a black box in the OH<sup>\*</sup>–Ni<sub>2.5</sub>Co<sub>5</sub>C<sub>2</sub>O<sub>4</sub> (202) DOS), (f) projected density of states (PDOS) for O-2p<sub>z</sub>, Ni-d<sub>xy</sub>, Ni-d<sub>z</sub><sup>2</sup> and Ni-d<sub>x</sub><sup>2</sup>-y<sup>2</sup> of OH<sup>\*</sup>–Ni<sub>2.5</sub>Co<sub>5</sub>C<sub>2</sub>O<sub>4</sub> (202), and (g) DOS plots for different catalyst surfaces. The thick red bar indicates the position of the d-band centre ( $E_d$ ) on catalyst surfaces.



–1.50, –1.37, –1.26 and –1.07 eV respectively for  $\text{Ni}_{2.5}\text{Co}_5\text{C}_2\text{O}_4$  (202),  $\text{CoC}_2\text{O}_4$  (202),  $\text{NiCo}_2\text{O}_4$  (311) and  $\text{NiC}_2\text{O}_4$  (202) surfaces (Fig. 5g) which vividly shows that the DBC gradually shifts towards the Fermi level from  $\text{Ni}_{2.5}\text{Co}_5\text{C}_2\text{O}_4$  to the  $\text{NiC}_2\text{O}_4$  (202) surface. The closer the DBC to the Fermi level, the stronger will be the adsorption of OH and hence deterioration of OER activity. This finding overwhelmingly supports our conclusion that the  $\text{Ni}_{2.5}\text{Co}_5\text{C}_2\text{O}_4$  catalyst is the best surface for the OER with weaker OH adsorption ability while  $\text{NiC}_2\text{O}_4$  is the least active with stronger OH binding ability. The present study highlights the benefit of nickel–cobalt oxalate over nickel–cobalt oxide for the alkaline OER process. We also believe that the use of oxalate ligand could be a promising strategy for the fabrication of new-generation electrocatalysts for electrochemical water oxidation in alkaline medium.

### 3. Conclusions

In summary, nickel–cobalt oxalate ( $\text{Ni}_{2.5}\text{Co}_5\text{C}_2\text{O}_4$ ) based block-like nanostructures were prepared by a wet-chemical technique in an aqueous medium and further treated by calcination at 350 °C for the synthesis of nickel cobalt oxide ( $\text{NiCo}_2\text{O}_4$ ). The preparation method was optimized in terms of Ni/Co ratio, oxalic acid amount, reaction temperature and time. The working electrode fabrication was performed on carbon paper as the substrate surface maintaining an optimum loading of the electrocatalyst. Next,  $\text{Ni}_{2.5}\text{Co}_5\text{C}_2\text{O}_4$  achieves 10 mA cm<sub>geo</sub><sup>–2</sup> with 330 mV overpotential, whereas  $\text{NiCo}_2\text{O}_4$  requires 410 mV for the same. The comparative study suggests the best electrochemical catalytic efficiency for  $\text{Ni}_{2.5}\text{Co}_5\text{C}_2\text{O}_4$ , and that can be attributed to lower charge transfer resistance, more changes in double layer capacitance during precondition in alkaline medium, and high surface coverage. DFT study reveals that comparatively weaker OH adsorption as well as favourable d-band centre (DBC) position makes the  $\text{Ni}_{2.5}\text{Co}_5\text{C}_2\text{O}_4$  catalyst the best surface for the OER compared to individual  $\text{CoC}_2\text{O}_4$  and  $\text{NiC}_2\text{O}_4$  as well as well studied  $\text{NiCo}_2\text{O}_4$ . This report thoroughly compares the activity of  $\text{Ni}_{2.5}\text{Co}_5\text{C}_2\text{O}_4$  and  $\text{NiCo}_2\text{O}_4$  for the alkaline OER process and highlights the benefit of  $\text{Ni}_{2.5}\text{Co}_5\text{C}_2\text{O}_4$  over  $\text{NiCo}_2\text{O}_4$ . The prudent choice of the oxalate based ligand-assisted synthetic approach could be used for other transition metals to execute bulk-scale alkaline water oxidation for a clean ecosystem and sustainable living.

### Conflicts of interest

There are no conflicts to declare.

### Acknowledgements

The author Sourav Ghosh would like to acknowledge the Department of Science and Technology (DST), India, for providing National Postdoctoral Fellowship (PDF/2017/001728/ES). RJ thanks IACS and DST. For their fellowships, HRI, GT, and HVSRMK thank UGC, RGNF UGC and DST-Inspire, respectively. The authors also acknowledge IISER Kolkata for instrumental facilities (including “TEM, DST-FIST facility,

IISER, Kolkata, India” for providing electron microscopy), “DST and SAIF, IIT Bombay” for ICP-AES analysis and IACS for XPS facility. R. J. thanks IACS and A. D. acknowledges DIA-SERB for funding computational resources. Dr Sourav Ghosh also acknowledges Technical Research Centre project (AI/1/64/SNB/2014) of S. N. Bose National Centre for Basic Sciences, Kolkata, India, for financial support. Dr Sourav Ghosh also thanks Dr Subhra Jana, Dr Mohua Chakraborty, Dr Saptarshi Pal, Ayan Mondal and Ruma Ghosh for helpful suggestions.

### References

- 1 A. Sivanantham, P. Ganesan, A. Vinu and S. Shanmugam, Surface Activation and Reconstruction of Non-Oxide-Based Catalysts Through In Situ Electrochemical Tuning for Oxygen Evolution Reactions in Alkaline Media, *ACS Catal.*, 2020, **10**, 463.
- 2 D. Li, J. Sun, R. Ma and J. Wei, High-efficient and Low-cost H<sub>2</sub> Production by Solar-driven Photo-thermo-reforming of Methanol with CuO Catalyst, *ES Energy Environ.*, 2020, **9**, 82.
- 3 P. Yang, H. Zhao, Y. Yang, P. Zhao, X. Zhao and L. Yang, Fabrication of N, P-Codoped Mo<sub>2</sub>C/Carbon Nanofibers Via Electrospinning as Electrocatalyst for Hydrogen Evolution Reaction, *ES Mater. Manuf.*, 2020, **7**, 34.
- 4 Y. Lv, L. Zhu, H. Xu, L. Yang, Z. Liu, D. Cheng, X. Cao, J. Yun and D. Cao, Core/Shell Template-Derived Co, N-Doped Carbon Bifunctional Electrocatalysts for Rechargeable Zn-Air Battery, *Eng. Sci.*, 2019, **7**, 26.
- 5 Z. Cai, P. Wang, J. Yang and X. Wang, Update on Recent Designing Strategies of Transition Metal-Based Layered Double Hydroxides Bifunctional Electrocatalysts, *ES Energy Environ.*, 2019, **5**, 22.
- 6 J. Suntivich, K. J. May, H. A. Gasteiger, J. B. Goodenough and Y. A. Shao-Horn, Perovskite Oxide Optimized for Oxygen Evolution Catalysis from Molecular Orbital Principles, *Science*, 2011, **334**, 1383.
- 7 M. Chatti, A. M. Glushenkov, T. Gengenbach, G. P. Knowles, T. C. Mendes, A. V. Ellis, L. Spiccia, R. K. Hocking and A. N. Simonov, Highly Dispersed and Disordered Nickel–Iron Layered Hydroxides and Sulphides: Robust and High-Activity Water Oxidation Catalysts, *Sustainable Energy Fuels*, 2018, **2**, 1561.
- 8 Z. P. Wu, X. F. Lu, S. Q. Zang and X. W. Lou, Non-Noble-Metal-based Electrocatalysts toward the Oxygen Evolution Reaction, *Adv. Funct. Mater.*, 2020, **30**, 1910274.
- 9 D. Xu, M. B. Stevens, Y. Rui, G. DeLuca, S. W. Boettcher, E. Reichmanis, Y. Li, Q. Zhang and H. Wang, The Role of Cr Doping in NiFe Oxide/(oxy)hydroxide Electrocatalysts for Oxygen Evolution, *Electrochim. Acta*, 2018, **265**, 10.
- 10 S. Jin, Are Metal Chalcogenides, Nitrides, and Phosphides Oxygen Evolution Catalysts or Bifunctional Catalysts?, *ACS Energy Lett.*, 2017, **2**, 1937.
- 11 D. Y. Chung, S. W. Jun, G. Yoon, H. Kim, J. M. Yoo, K.-S. Lee, T. Kim, H. Shin, A. K. Sinha, S. G. Kwon, K. Kang, T. Hyeon and Y.-E. Sung, Large-Scale Synthesis of Carbon–Shell-Coated FeP Nanoparticles for Robust Hydrogen Evolution Reaction Electrocatalyst, *J. Am. Chem. Soc.*, 2017, **139**, 6669.



- 12 N.-T. Suen, S.-F. Hung, Q. Quan, N. Zhang, Y.-J. Xu and H. M. Chen, Electrocatalysis for the Oxygen Evolution Reaction: Recent Development and Future Perspectives, *Chem. Soc. Rev.*, 2017, **46**, 337.
- 13 C. Zhang, Y. Xie, H. Deng, C. Zhang, J. Su and J. Lin, Nitrogen Doped Coal with High Electrocatalytic Activity for Oxygen Reduction Reaction, *Eng. Sci.*, 2019, **8**, 39.
- 14 H. Wu, Y. Zhang, R. Yin, W. Zhao, X. Li and L. Qian, Magnetic negative permittivity with dielectric resonance in random  $\text{Fe}_3\text{O}_4$ @graphene-phenolic resin composites, *Adv. Compos. Hybrid Mater.*, 2018, **1**, 168.
- 15 P. Xie, Y. Liu, M. Feng, M. Niu, C. Liu, N. Wu, K. Sui, R. R. Patil, D. Pan, Z. Guo and R. Fan, Hierarchically porous Co/C nanocomposites for ultralight high-performance microwave absorption, *Adv. Compos. Hybrid Mater.*, 2021, **4**, 173.
- 16 J. Qi, W. Zhang and R. Cao, Aligned Cobalt-Based  $\text{Co}@\text{CoO}_x$  Nanostructures for Efficient Electrocatalytic Water Oxidation, *Chem. Commun.*, 2017, **53**, 9277.
- 17 H. Yu, L. Yang, D. Cheng and D. Cao, Zeolitic-imidazolate Framework (ZIF)@ZnCo-ZIF Core-shell Template-derived Co, N-doped Carbon Catalysts for Oxygen Reduction Reaction, *Eng. Sci.*, 2018, **3**, 54.
- 18 G. Li, C. Dang, Y. Hou, F. Dang, Y. Fan and Z. Guo, Experimental and Theoretical Characteristic of Single Atom Co-N-C Catalyst for  $\text{Li}-\text{O}_2$  Batteries, *Eng. Sci.*, 2020, **10**, 85.
- 19 P. Chen, K. Xu, Z. Fang, Y. Tong, J. Wu, X. Lu, X. Peng, H. Ding, C. Wu and Y. Xie, Metallic  $\text{Co}_4\text{N}$  Porous Nanowire Arrays Activated by Surface Oxidation as Electrocatalysts for the Oxygen Evolution Reaction, *Angew. Chem.*, 2015, **127**, 14923.
- 20 S. Ghosh, G. Tudu, A. Mondal, S. Ganguli, H. R. Inta and V. Mahalingam, Inception of  $\text{Co}_3\text{O}_4$  as Microstructural Support to Promote Alkaline Oxygen Evolution Reaction for  $\text{Co}_{0.85}\text{Se}/\text{Co}_9\text{Se}_8$  Network, *Inorg. Chem.*, 2020, **59**, 17326.
- 21 A. Mendoza-Garcia, D. Su and S. Sun, Sea Urchin-like Cobalt-Iron Phosphide as an Active Catalyst for Oxygen Evolution Reaction, *Nanoscale*, 2016, **8**, 3244.
- 22 S. Klemenz, J. Schuch, S. Hawel, A.-M. Zieschang, B. Kaiser, W. Jaegermann and B. Albert, Synthesis of a Highly Efficient Oxygen-Evolution Electrocatalyst by Incorporation of Iron into Nanoscale Cobalt Borides, *ChemSusChem*, 2018, **11**, 3150.
- 23 Y. Xue, Y. Wang, H. Liu, X. Yu, H. Xue and L. Feng, Electrochemical Oxygen Evolution Reaction Catalyzed by a Novel Nickel-Cobalt-Fluoride Catalyst, *Chem. Commun.*, 2018, **54**, 6204.
- 24 P. K. Katkar, S. J. Marje, S. B. Kale, A. C. Lokhande, C. D. Lokhande and U. M. Patil, Synthesis of Hydrous Cobalt Phosphate Electro-catalysts by a Facile Hydrothermal Method for Enhanced Oxygen Evolution Reaction: Effect of Urea Variation, *CrystEngComm*, 2019, **21**, 884.
- 25 S. Ganguli, S. Das, S. Kumari, H. R. Inta, A. K. Tiwari and V. Mahalingam, Effect of Intrinsic Properties of Anions on the Electrocatalytic Activity of  $\text{NiCo}_2\text{O}_4$  and  $\text{NiCo}_2\text{O}_x\text{S}_{4-x}$  Grown by Chemical Bath Deposition, *ACS Omega*, 2018, **3**, 9066.
- 26 J. S. Yeoh, C. F. Armer and A. Lowe, Transition Metal Oxalates as Energy Storage Materials: A review, *Mater. Today Energy*, 2018, **9**, 198.
- 27 J. W. Kim, J. K. Lee, D. Phihusut, Y. Yi, H. J. Lee and J. Lee, Self-Organized One-Dimensional Cobalt Compound Nanostructures from  $\text{CoC}_2\text{O}_4$  for Superior Oxygen Evolution Reaction, *J. Phys. Chem. C*, 2013, **117**, 23712.
- 28 D. Phihusut, J. D. Ocon, B. Jeong, J. W. Kim, J. K. Lee and J. Lee, Gently Reduced Graphene Oxide Incorporated into Cobalt Oxalate Rods as Bifunctional Oxygen Electrocatalyst, *Electrochim. Acta*, 2014, **140**, 404.
- 29 X. Liu, J. Jiang and L. Ai, Non-Precious Cobalt Oxalate Microstructures as Highly Efficient Electrocatalysts for Oxygen Evolution Reaction, *J. Mater. Chem. A*, 2015, **3**, 9707.
- 30 H. B. Wu, H. Pang and X. W. Lou, Facile Synthesis of Mesoporous  $\text{Ni}_{0.3}\text{Co}_{2.7}\text{O}_4$  Hierarchical Structures for High-Performance Supercapacitors, *Energy Environ. Sci.*, 2013, **6**, 3619.
- 31 L. Wang, R. Zhang, Y. Jiang, H. Tian, Y. Tan, K. Zhu, Z. Yu and W. Li, Interfacial synthesis of micro-cuboid  $\text{Ni}_{0.55}\text{Co}_{0.45}\text{C}_2\text{O}_4$  solid solution with enhanced electrochemical performance for hybrid supercapacitors, *Nanoscale*, 2019, **11**, 13894.
- 32 S. Ghosh, M. Roy and M. K. Naskar, A Facile Soft Chemical Synthesis of Cube-Shaped Mesoporous  $\text{CuO}$  with Microcarpet-Like Interior, *Cryst. Growth Des.*, 2014, **14**, 2977.
- 33 H.-J. Oh, C.-H. Jo, C.-S. Yoon, H. Yashiro, S.-J. Kim, S. Passerini, Y.-K. Sun and S.-T. Myung, Nickel Oxalate Dihydrate Nanorods Attached to Reduced Graphene Oxide Sheets as a High Capacity Anode for Rechargeable Lithium Batteries, *NPG Asia Mater.*, 2016, **8**, e270-e277.
- 34 M. S. Loeian, D. A. Ziolkowska, F. Khosravi, J. B. Jasinski and B. Panchapakesan, Exfoliated  $\text{WS}_2$ -Nafion Composite Based Electromechanical Actuators, *Sci. Rep.*, 2017, **7**, 14599.
- 35 S. Ghosh, H. R. Inta, S. Ganguli, G. Tudu, H. V. S. R. M. Koppisetti and V. Mahalingam,  $\text{MoO}_2$  as a Propitious "Pore Forming Additive" for Boosting Water Oxidation Activity of Cobalt Oxalate Microrods, *J. Phys. Chem. C*, 2020, **124**, 20010.
- 36 P. W. Menezes, A. Indra, D. González-Flores, N. R. Sahraie, I. Zaharieva, M. Schwarze, P. Strasser, H. Dau and M. Driess, High-Performance Oxygen Redox Catalysis with Multifunctional Cobalt Oxide Nanochains: Morphology Dependent Activity, *ACS Catal.*, 2015, **5**, 2017.
- 37 S. Ganguli, S. Ghosh, S. Das and V. Mahalingam, Inception of Molybdate as a "Pore Forming Additive" to Enhance the Bifunctional Electrocatalytic Activity of Nickel and Cobalt based Mixed Hydroxides for Overall Water Splitting, *Nanoscale*, 2019, **11**, 16896.
- 38 Y. Wei, X. Ren, H. Ma, X. Sun, Y. Zhang, X. Kuang, T. Yan, H. Ju, D. Wu and Q. Wei,  $\text{CoC}_2\text{O}_4 \cdot 2\text{H}_2\text{O}$  Derived  $\text{Co}_3\text{O}_4$  Nanorods Array: A High-Efficiency 1D Electrocatalyst for Alkaline Oxygen Evolution Reaction, *Chem. Commun.*, 2018, **54**, 1533.



- 39 C. Wei and Z. J. Xu, The Comprehensive Understanding of  $10 \text{ mA cm}_{\text{geo}}^{-2}$  as an Evaluation Parameter for Electrochemical Water Splitting, *Small Methods*, 2018, **2**, 1800168.
- 40 C. Yang, C. Laberty-Robert, D. Batuk, G. Cibin, A. V. Chadwick, V. Pimenta, W. Yin, L. Zhang, J. Tarascon and A. Grimaud, Phosphate Ion Functionalization of Perovskite Surfaces for Enhanced Oxygen Evolution Reaction, *J. Phys. Chem. Lett.*, 2017, **8**, 3466.
- 41 A. Grimaud, O. Diaz-Morales, B. Han, W. T. Hong, Y. L. Lee, L. Giordano, K. A. Stoerzinger, M. T. M. Koper and Y. Shao-Horn, Activating Lattice Oxygen Redox Reactions in Metal Oxides to Catalyse Oxygen Evolution, *Nat. Chem.*, 2017, **9**, 457.
- 42 A. Bergmann, T. E. Jones, E. M. Moreno, D. Teschner, P. Chernev, M. Gliech, T. Reier, H. Dau and P. Strasser, Unified Structural Motifs of the Catalytically Active State of Co(Oxyhydr)-Oxides During the Electrochemical Oxygen Evolution Reaction, *Nat. Catal.*, 2018, **1**, 711.
- 43 Y. Yoon, B. Yan and Y. Surendranath, Suppressing Ion Transfer Enables Versatile Measurements of Electrochemical Surface Area for Intrinsic Activity Comparisons, *J. Am. Chem. Soc.*, 2018, **140**, 2397.
- 44 C. C. L. McCrory, S. Jung, I. M. Ferrer, S. M. Chatman, J. C. Peters and T. F. Jaramillo, Benchmarking Hydrogen Evolving Reaction and Oxygen Evolving Reaction Electrocatalysts for Solar Water Splitting Devices, *J. Am. Chem. Soc.*, 2015, **137**, 4347.
- 45 J. Xu, J. P. S. Sousa, N. E. Mordinova, J. D. Costa, D. Y. Petrovykh, K. Kovnir, O. I. Lebedev and Y. V. Kolen'ko, Al-Induced In Situ Formation of Highly Active Nanostructured Water-Oxidation Electrocatalyst Based on Ni-Phosphide, *ACS Catal.*, 2018, **8**, 2595.
- 46 C. Wei, R. Rao, J. Peng, B. Huang, I. E. L. Stephens, M. Risch, Z. J. Xu and Y. Shao-Horn, Recommended Particles and Benchmark Activity for Hydrogen and Oxygen Electrocatalysis in Water Splitting and Fuel Cells, *Adv. Mater.*, 2019, 1806296.
- 47 S. Ghosh, R. Das and M. K. Naskar, Morphologically Tuned Aluminum Hydrous Oxides and their Calcined Products, *J. Am. Ceram. Soc.*, 2016, **99**, 2273.
- 48 S. Ganguli, H. V. S. R. M. Koppisetti, S. Ghosh, T. Biswas and V. Mahalingam, Paradoxical Observance of "Intrinsic" and "Geometric" Oxygen Evolution Electrocatalysis in Phase-Tuned Cobalt Oxide/Hydroxide Nanoparticles, *ACS Appl. Nano Mater.*, 2019, **2**, 7957.
- 49 J. Saha, D. R. Chowdhury, P. Jash and A. Paul, Cobalt Phosphonates as Precatalysts for Water Oxidation: Role of Pore Size in Catalysis, *Chem.-Eur. J.*, 2017, **23**, 12519.
- 50 S. M. AlShehri, J. Ahmed, T. Ahamad, P. Arunachalam, T. Ahmad and A. Khan, Bifunctional Electro-Catalytic Performances of  $\text{CoWO}_4$  Nanocubes for Water Redox Reactions (OER/ORR), *RSC Adv.*, 2017, **7**, 45615.
- 51 J. A. Vigil, T. N. Lambert and B. T. Christensen, Cobalt Phosphide-Based Nanoparticles as Bifunctional Electrocatalysts for Alkaline Water Splitting, *J. Mater. Chem. A*, 2016, **4**, 7549.
- 52 X. Liu, Y. Yang and S. Guan, An Efficient Electrode Based on One-Dimensional  $\text{CoMoO}_4$  Nanorods for Oxygen Evolution Reaction, *Chem. Phys. Lett.*, 2017, **675**, 11.
- 53 Y. Cui, Y. Xue, R. Zhang, J. Zhang, X. Li and X. Zhu, Vanadium-Cobalt Oxyhydroxide Shows Ultralow Overpotential for the Oxygen Evolution Reaction, *J. Mater. Chem. A*, 2019, **7**, 21911.
- 54 L. Ai, X. Gao and J. Jiang, In Situ Synthesis of Cobalt Stabilized on Macroscopic Biopolymer Hydrogel as Economical and Recyclable Catalyst for Hydrogen Generation from Sodium Borohydride Hydrolysis, *J. Power Sources*, 2014, **257**, 213.
- 55 G. Kresse and J. Hafner, Ab Initio Molecular Dynamics for Liquid Metals, *Phys. Rev. B: Condens. Matter Mater. Phys.*, 1993, **4**, 558.
- 56 R. Subbaraman, D. Tripkovic, K.-C. Chang, D. Strmcnik, A. P. Paulikas, P. Hirunsit, M. Chan, J. Greeley, V. Stamenkovic and N. M. Markovic, Trends in Activity for the Water Electrolyser Reactions on 3d  $\text{M}(\text{Ni},\text{Co},\text{Fe},\text{Mn})$  Hydr(oxy)oxide Catalysts, *Nat. Mater.*, 2012, **11**, 550.
- 57 F. Song, L. Bai, A. Moysiadou, S. Lee, C. Hu, L. Liardet and X. Hu, Transition Metal Oxides as Electrocatalysts for the Oxygen Evolution Reaction in Alkaline Solutions: An Application-Inspired Renaissance, *J. Am. Chem. Soc.*, 2018, **140**, 7748.
- 58 S. J. Trasatti, Electrocatalysis by Oxides—Attempt at a Unifying Approach, *J. Electroanal. Chem. Interfacial Electrochem.*, 1980, **111**, 125.
- 59 S. Trasatti, Electrocatalysis in the Anodic Evolution of Oxygen and Chlorine, *Electrochim. Acta*, 1984, **29**, 1503.
- 60 P. Rüetschi and P. Delahay, Influence of Electrode Material on Oxygen Overvoltage: A Theoretical Analysis, *J. Chem. Phys.*, 1955, **23**, 556.
- 61 R. F. W. Bader, *Atoms in Molecules: A Quantum Theory*, Oxford University Press, Oxford, 1990.
- 62 G. Henkelman, A. Arnaldsson and H. Jónsson, A Fast and Robust Algorithm for Bader Decomposition of Charge Density, *Comput. Mater. Sci.*, 2006, **36**, 354.
- 63 R. Jana, C. Chowdhury, S. Malik and A. Datta,  $\text{Pt/Co}_3\text{O}_4$  Surpasses Benchmark Pt/C: An Approach Toward Next Generation Hydrogen Evolution Electrocatalyst, *ACS Appl. Energy Mater.*, 2019, **2**, 5613.
- 64 M. Mavrikakis, B. Hammer and J. K. Nørskov, Effect of Strain on the Reactivity of Metal Surfaces, *Phys. Rev. Lett.*, 1998, **81**, 2819.
- 65 H. Lv, Z. Xi, Z. Chen, S. Guo, Y. Yu, W. Zhu, Q. Li, X. Zhang, M. Pan, G. Lu, S. Mu and S. A. Sun, New Core/Shell  $\text{NiAu}/\text{Au}$  Nanoparticle Catalyst with Pt-like Activity for Hydrogen Evolution Reaction, *J. Am. Chem. Soc.*, 2015, **137**, 5859.

